High-Frequency Waves Driven by Agyrotropic Electrons Near the Electron Diffusion Region

Kyunghwan Dokgo[1] , Kyoung-Joo Hwang[1] , James L. Burch[1] , Peter H. Yoon[2,3,4] , Daniel B. Graham[5] , and Wenya Li[5,6]

[1]Southwest Research Institute, San Antonio, TX, USA, [2]Institute for Physical Science and Technology, University of Maryland, College Park, MD, USA, [3]Korea Astronomy and Space Science Institute, Daejeon, South Korea, [4]School of Space Research, Kyung Hee University, Yongin, South Korea, [5]Swedish Institute of Space Physics, Uppsala, Sweden, [6]State Key Laboratory of Space Weather, National Space Science Center, Chinese Academy of Sciences, Beijing, China

Abstract National Aeronautics and Space Administration's Magnetosphere Multiscale mission reveals that agyrotropic electrons and intense waves are prevalently present in the electron diffusion region. Prompted by two distinct Magnetosphere Multiscale observations, this letter investigates by theoretical means and the properties of agyrotropic electron beam-plasma instability and explains the origin of different structures in the wave spectra. The difference is owing to the fact that in one instance, a continuous beam mode is excited, while in the other, discrete Bernstein modes are excited, and the excitation of one mode versus the other depends on physical input parameters, which are consistent with observations. Analyses of dispersion relations show that the growing mode becomes discrete when the maximum growth rate is lower than the electron cyclotron frequency. Making use of particle-in-cell simulations, we found that the broadening angle Δ in the gyroangle space is also an important factor controlling the growth rate. Ramifications of the present finding are also discussed.

Plain Language Summary Magnetospheric Multiscale mission has observed magnetic reconnection process, which converts magnetic energy to kinetic energy of charged particles. Extremely rapid time scale data reveal that electron scale high-frequency waves exist near the electron diffusion region of magnetic reconnection. Recently, two different types of waves observed; one is discrete electron-Bernstein waves, and the other is continuous beam modes. In this study, we formulated a unified theory for both types of waves. Comparing Magnetosphere Multiscale observations, the theory, and particle-in-cell simulations, this study shows that the same cause (agyrotropic electrons) can make two different wave structures depending on plasma parameters. The condition that the maximum growth rate of instabilities equals the electron cyclotron frequency can be considered as a threshold of the transition from discrete electron Bernstein waves to continuous beam modes.

1. Introduction

Magnetic reconnection is a fundamental physical process in plasmas. It converts magnetic energy into kinetic energy of charged particles by reconfiguring topologies of magnetic field lines. The recently launched National Aeronautics and Space Administration's Magnetosphere Multiscale (MMS) mission enables investigations of electron-scale phenomena in reconnection sites as the four MMS spacecraft provide high-resolution data (Burch et al., 2016). Specifically, they reveal details of the electron diffusion region (EDR) of magnetic reconnection. In this region, electrons are demagnetized. Consequently, the kinetic physics of electrons becomes dominant (Birn et al., 2001; Vasyliunas, 1975).

One of most important findings is the existence of crescent-shaped agyrotropic electrons in EDRs (Burch et al., 2016). They are generated by meandering motions of electrons (Hesse et al., 2014; Scudder & Daughton, 2008), and their structures have been intensely studied (Bessho et al., 2014; Egedal et al., 2016; Shuster et al., 2015). Agyrotropic electrons play crucial roles in generating the reconnection electric field via off-diagonal electron pressure tensor terms (Hesse & Winske, 1994; Hesse et al., 2014; Lyons & Pridmore-Brown, 1990).

Moreover, the MMS spacecraft observes that agyrotropic electrons generate various waves, for example, Langmuir waves, upper-hybrid waves (Burch et al., 2018, 2019; Dokgo et al., 2019; Graham et al., 2017;
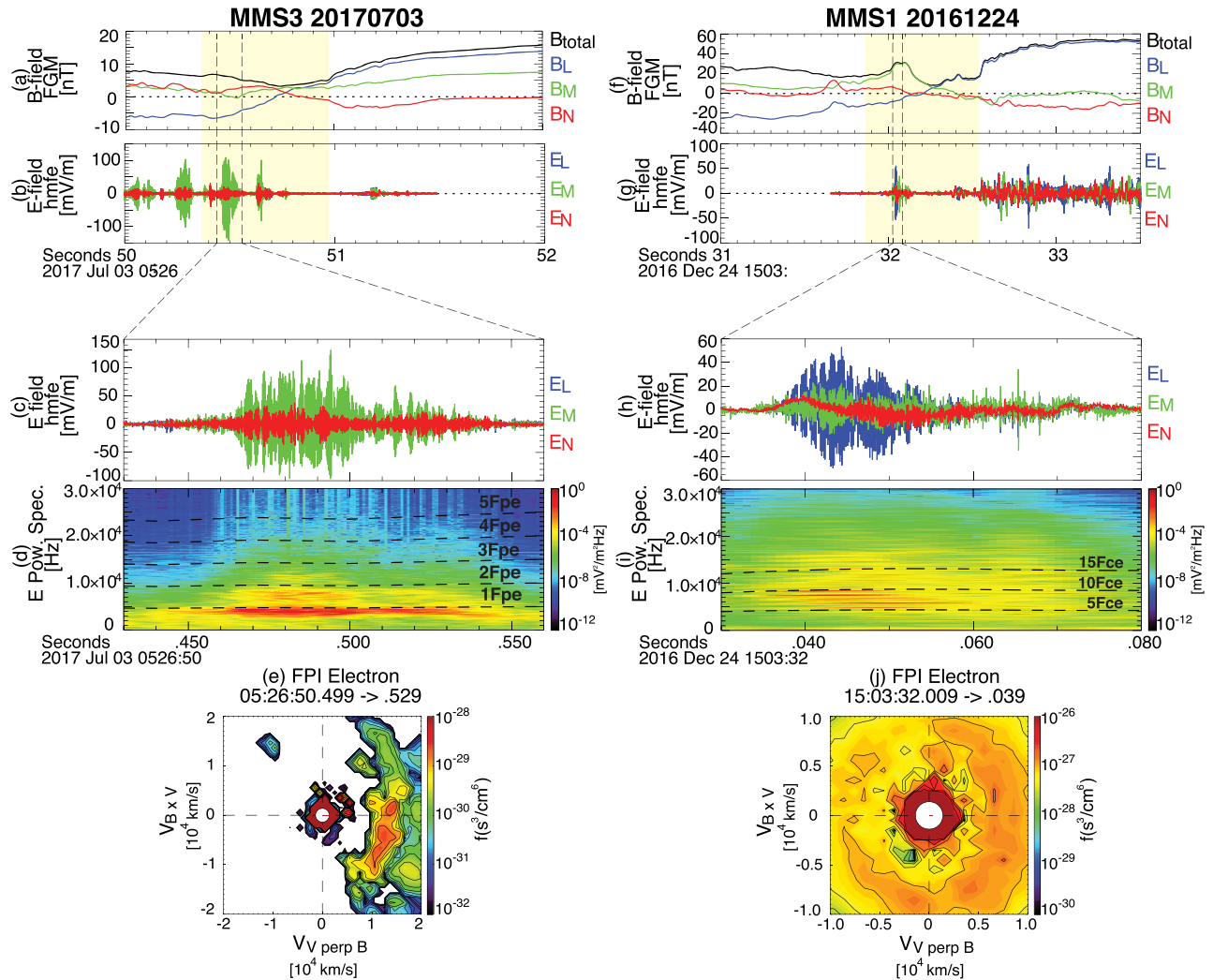
Figure 1. MMS Observations of (left) Event 1 and (right) Event 2. (a, f) Magnetic field, (b, g) electric field, (c, h) burst of HFWs, (d, i) E field spectrum, and (e, j) electron distribution in the perpendicular plane. Black dashed lines in (d) and (i) are $nF_{pe}, n = 1, 2, 3, \ldots$ ($F_{pe} \simeq 4.8$ kHz) and $nF_{ce}, n = 5, 10, 15$ ($F_{ce} \simeq 0.86$ kHz), respectively.

Tang et al., 2019), and electron Bernstein waves (Graham et al., 2018; Li et al., 2020). As such waves are generated near EDRs, they could significantly affect the environment of EDRs via wave-particle interactions. They can energize and diffuse electrons and are also a possible source of anomalous resistivity or viscosity that supports the reconnection electric field. Previous studies of agyrotropic-beam instability are incomplete in that either agyrotropy is ignored or that effects of magnetic field are not included. This letter rectifies such shortcomings and test the theory against recent MMS observations.

We study two MMS events when the spacecraft observed agyrotropic electrons near EDRs. These events show two different types of high-frequency wave (HFW) activities. By employing an electrostatic linear dispersion relation, which is appropriate for analyzing instabilities driven by agyrotropic electrons, we accurately interpret the observed wave phenomena in terms of the agyrotropic beam-plasma instability. Particle-in-cell (PIC) simulations show that the broadening angle Δ is also an important factor, which can change the growth rate by more than an order of magnitude and eventually affect the wave structure generated. In this study, we use burst mode data from the fluxgate magnetometer (Russell et al., 2016), the electric field double probes (Ergun et al., 2016; Lindqvist et al., 2016), and the fast plasma investigation (Pollock et al., 2016).

2. Two Different Types of Waves in MMS Observations

Figure 1 presents MMS observations of two events: (left) the Event 1 on 3 July 2017 near 05:26:50 UT (Burch et al., 2019; Dokgo et al., 2019) in the inflow region near the EDR of the symmetric reconnection at the magnetotail and (right) the Event 2 on 24 December 2016 near 15:30:32 UT (Li et al., 2020) in the electron exhaust region of the asymmetric reconnection at the dayside magnetopause. The yellow-shaded regions in the top panels are in or near the EDR. The field data are presented in LMN coordinates calculated by minimum variance analysis (Paschmann et al., 1998) of the magnetic field, which are $\mathbf{L} = [0.97, -0.25, 0.04]$, $\mathbf{M} = [0.23, 0.93, 0.29]$, $\mathbf{N} = [-0.11, -0.27, 0.96]$ for Event 1 and $\mathbf{L} = [0.09, 0.08, 0.99]$, $\mathbf{M} = [0.23, -0.97, 0.06]$, $\mathbf{N} = [0.97, 0.22, -0.10]$ for Event 2 in geocentric solar ecliptic coordinates. ($\mathbf{L}$: reconnecting B direction, $\mathbf{M}$: out-of-plane guide field direction, and $\mathbf{N}$: normal direction)

For Event 1, MMS spacecraft crossed the EDR when B_L reverses from negative to positive (Figure 1a) (Dokgo et al., 2019). As shown in Figure 1b, HFWs are observed in the E field before the EDR crossing. We enlarge the interval exhibiting the most intense wave burst (Figure 1c) and present the power spectrum in Figure 1d, where horizontal lines corresponding to integer multiples of electron plasma frequency, nF_{pe}, $n = 1, 2, 3, \ldots$, ($F_{pe} \simeq 4.8$ kHz) are indicated. Figure 1e shows agyrotropic electrons in the perpendicular plane. Ignoring effects of the magnetic field on the agyrotropic beam, Burch et al. (2019) found that the linear beam-plasma interaction between core and agyrotropic electrons generate the fundamental mode near F_{pe}.

We present the observation for Event 2 in the same format (Figures 1f–1j). HFWs observed in the electron exhaust region are shown in Figure 1g. Note that in this case multiple electron cyclotron harmonics, nF_{ce}, $n = 5, 10, 15$, ($F_{ce} \simeq 0.86$ kHz) are indicated with horizontal dashed lines in Figure 1i, together with the wave power spectrum. Highly discrete wave signals at multiples of F_{ce} characterize this event. As shown in Figure 1j, the agyrotropic electrons are also observed in this event. By assuming a gyrotropic ring electron distribution, Li et al. (2020) interpreted such a feature in terms of the customary electron Bernstein mode excitation.

While dispersion relations calculated by Burch et al. (2019) and Li et al. (2020) for each event show a superficial agreement with observations, strictly speaking both of their assumptions are not supported by MMS observations, since observations show agyrotropy of electron distributions with the ambient magnetic field. Moreover, as the free energy source for both events resides in the common agyrotropic nature of the electron distribution, the only difference being plasma parameters, it is desirable to formulate a unified theory that may account for both events. In the present letter we calculate the dispersion relation including effects of agyrotropic electrons and the magnetic field, so as to offer unified explanations for the two events showcased in Figure 1.

3. A Unified Kinetic Theory for Both Types of Waves

Derivations of electrostatic dispersion relations are based upon the approach taken by Romeiras and Brinca (1999) with modifications. Cylindrical coordinates $(v_x, v_\perp, \psi)$ are used, where the ambient magnetic field is directed along x axis and ψ is the gyrophase angle in perpendicular y-z plane with the y axis defines $\psi = 0$. The agyrotropic electrons propagate to the y direction.

The zeroth-order distribution F_{0s} is given by $F_{0s}(v_x, v_\perp, \psi) = 2\pi W_s(v_x, v_\perp) \Phi_s(\psi)$, where W_s is a thermal ring Maxwellian $W_s(v_x, v_\perp) = L_s^{-1} \exp\left[-v_x^2/v_{ts}^2 - (v_\perp - V_{Ds})^2/(A_s v_{ts}^2)\right]$ and the subscript s indicates species: eM (electron Maxwellian), pM (proton Maxwellian), and b (agyrotropic beam). M stands for Maxwellian. Thermal speed is defined by $v_{ts} \equiv \sqrt{2T_s/m_s}$, where m_s and T_s are mass and temperature, respectively. $A_s \equiv T_{\perp s}/T_{xs}$ is the anisotropy. V_{Ds} is a perpendicular drift speed; thus, $V_{DeM} = V_{DpM} = 0$. Note that Romeiras and Brinca (1999) considered only $V_{Ds} = 0$. L_s is the normalization factor, which is given for each species by $L_{sM} = A_s \left(\sqrt{\pi} v_{tsM}\right)^3$, and $L_b = A_b \left(\sqrt{\pi} v_{tb}\right)^3 \left\{e^{-u_b^2} + \sqrt{\pi} u_b \left[1 + \text{Erf}\left(u_b\right)\right]\right\}$, where $u_b = V_{Db}/(\sqrt{A_b} v_{tb})$. We assume gyrotropic cores and monoenergetic beam, so it is given by $\Phi_{sM} = 1/(2\pi)$ and $\Phi_b = \delta(\psi)$, following Romeiras and Brinca (1999). Note that $\delta(\psi)$ is a periodic delta function, known as the Dirac comb, because ψ is a 2π-periodic variable. We consider that all perturbations propagate along y axis, so the first-order perturbation in $N_{0s} F_{0s}$ (N_{0s} being the density) can be expressed in the form $f_s(\vec{r}, \vec{v}, t) = \bar{f}_s(\vec{v}) \exp\left[i(ky - \omega t)\right]$.
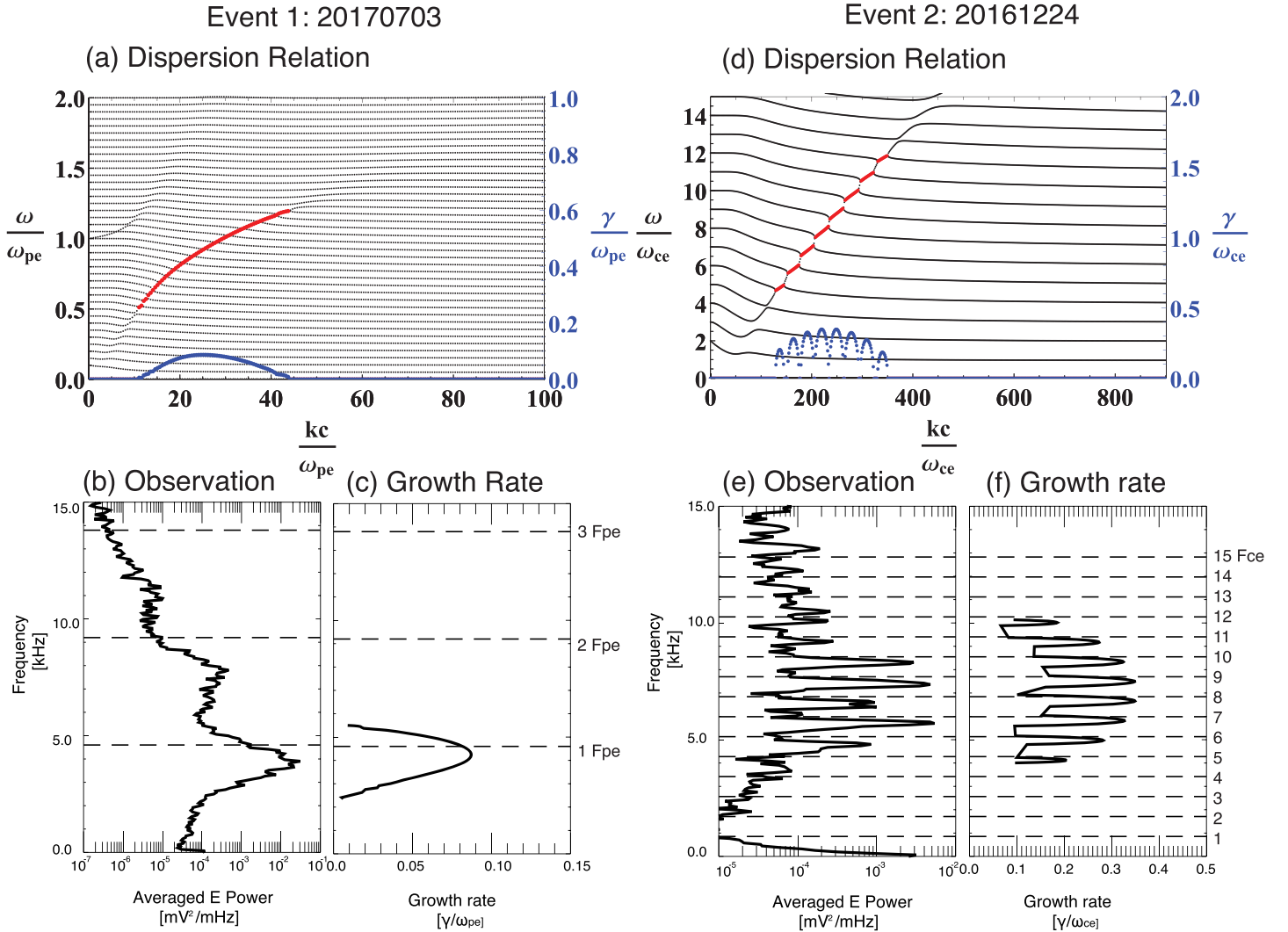
Figure 2. Comparisons between MMS observations and theory for (left) Event 1 and (right) Event 2. (a, d) Dispersion relations and growth rates in $\omega - k$ space by equation (1) using plasma parameters obtained from MMS data, (b, e) averaged powers of observed electron field data, and (c, f) growth rates computed from theory.

Calculating the perturbed charge density ρ_s and inserting to Poisson equation, we may derive the dispersion relation:

$$
\begin{aligned}
0 = 1 - & \sum_{s=eM,pM} \left[\left(\frac{\omega_{ps}}{\omega_{cs}} \right)^2 \frac{e^{-\Lambda_s}}{\Lambda_s} \sum_{n=-\infty}^{\infty} \frac{n I_n(\Lambda_s)}{\omega_s - n} \right] \\
& - \left(\frac{\omega_{pb}}{\omega_{cb}} \right)^2 \frac{\pi^{3/2} A_b v_{tb}^3}{2\pi L_b \Lambda_b} \sum_{m=-\infty}^{\infty} \frac{1}{\omega_b - m} \\
& \times \int_0^{\infty \times \Omega_b} d\xi_b J_m(\xi_b) \left[\frac{\xi_b(\xi_b - \eta_b)}{\Lambda_b} - 1 \right] e^{-\frac{(\xi_b - \eta_b)^2}{2\Lambda_b}}.
\end{aligned}
\tag{1}
$$

where $\omega_{cs} = q_s B_0 / m_s$ is the gyrofrequency, q_s is the charge, $\omega_{ps} = N_{0s} q_s^2 / (\epsilon_0 m_s)$ is the plasma frequency for species s, ϵ_0 is the vacuum permittivity, I_n is the modified Bessel function of the first kind of order n, J_m is the Bessel function of the first kind of order m, $\omega_s = \omega / \omega_{cs}$, $\xi_s = k v_\perp / \omega_{cs}$, $\Lambda_s = k^2 A_s v_{ts}^2 / (2\omega_{cs}^2)$, and $\eta_s = k V_{Ds} / \omega_{cs}$. Solving equation (1) leads to the dispersion relations describing wave frequency and growth for instability excited by agyrotropic beams.

Making use of equation (1) and plasma parameters obtained from two MMS events (Burch et al., 2019; Dokgo et al., 2019; Li et al., 2020), we calculate dispersion relations. We focus on electron interactions, so
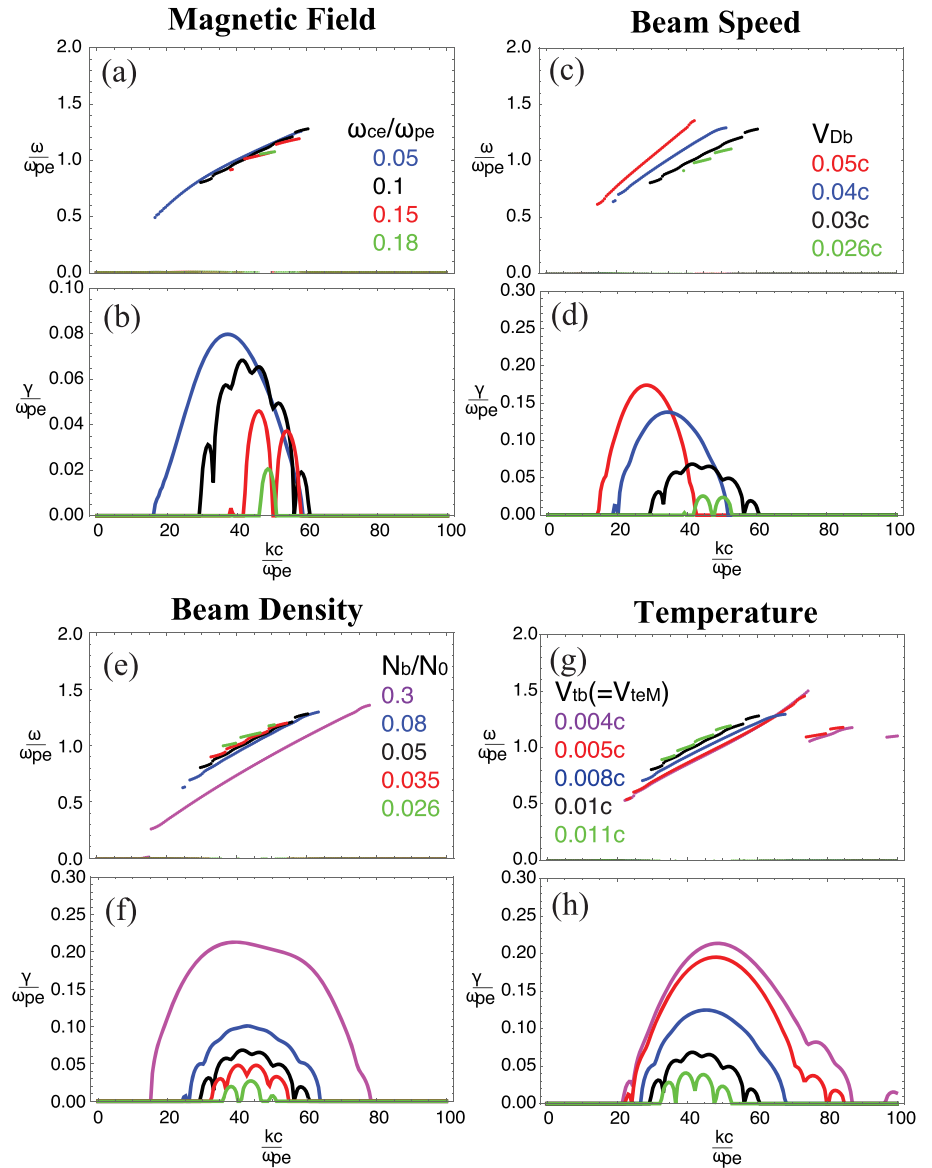
Figure 3. Dispersion relations (upper panel) and growth rates (lower panel) derived by changing (a, b) ω_{ce}/ω_{pe} ratio, (c, d) beam drift speed, (e, f) beam density, and (g, h) temperatures of beam and core.

components of electron core and beam are considered while assuming the ions are immobile. Parameters are given by $N_b = 0.085N_0$, $\omega_{ce} = -0.05\omega_{pe}$, $A_b = 4.0$, $A_{eM} = 1.0$, $V_{Db} = 0.0433c$, $v_{tb} = 0.0117c$, and $v_{teM} = 0.0117c$ for Event 1 and $N_b = 0.54N_0$, $\omega_{ce} = -0.0333\omega_{pe}$, $A_b = 3.2$, $A_{eM} = 2.04$, $V_{Db} = 0.02c$, $v_{tb} = 0.0233c$, and $v_{teM} = 0.01c$ for Event 2, where c is the speed of light, N_0 is the total density, and $\omega_{pe}^2 \equiv \omega_{peM}^2 + \omega_{pb}^2$. We have summed the second and third terms in equation (1) from $n, m = -100$ to $+100$ in order to fully include effects of the magnetic field above the electron plasma frequency for both cases.

Figure 2 shows dispersion relations and comparisons between observations. Figure 2a is the dispersion relation corresponding to Event 1 in $\omega - k$ space. The horizontal axis represents the wave number kc/ω_{pe}, while the vertical axis is the frequency ω/ω_{pe}. Black lines are the real parts, while the blue line is the imaginary part (growth rate). The red line emphasizes the growing part of the dispersion curves where growth rates are positive. The horizontal black curves (near integer multiples of $F_{ce} = 0.05F_{pe}$) arise from including the effects of ambient magnetic field, which in the unmagnetized plasma theory are absent (Burch et al., 2019; Dokgo et al., 2019). For Event 1, the cyclotron harmonics are closely packed so that the growth rate envelop forms a rather smooth and continuous curve. As a result, the dispersion relation is almost the same as the

unmagnetized analysis carried out by Burch et al. (2019). Figure 2b shows the averaged power of E spectrum as observed by MMS. The frequency range of the fundamental mode agrees with the growth rate converted to the real frequency domain shown in Figure 2c. As already explained in Dokgo et al. (2019), higher harmonics are results of nonlinear mode excitations, which is beyond scope of the present linear theory.

Effects of the ambient magnetic field are very important for Event 2. In this case, gyroharmonic separations in frequency space are sufficiently wide so that the growth rate envelop features distinct local maxima. This is the result of beam mode intersecting horizontal cyclotron modes, which leads to the growth rate curve becoming discretized. This is shown in Figure 2d, where horizontal and vertical axes are normalized by ω_{ce} and ω_{ce}/c, respectively. Indeed, the growth rate has local maxima near integer multiples of F_{ce}, which resembles the electron Bernstein waves, but it is important to emphasize that the free energy source is primarily provided by the agyrotropic electrons. The averaged power spectrum of E (Figure 2e) and the theoretical growth rate (Figure 2f) agree with each other; the most intense modes are in the range from $4F_{ce}$ to $10F_{ce}$, and each mode is located between nF_{ce} and (n+1)F_{ce}. We note that the frequency range of this event is from 0.1 to 0.3 in the unit of F_{pe} and this is very low compared to Event 1. The frequency range is downshifted from $\sim F_{pe}$ because of high beam density (Cairns, 1989).

We carry out analyses of general properties of agyrotropic beam-plasma interactions. As a reference case, we use input parameters given by $N_b = 0.05N_0$, $V_{Db} = 0.03c$, $\omega_{ceM} = \omega_{cb} = -0.1\omega_{pe}$, $\omega_{pe}^2 \equiv \omega_{peM}^2 + \omega_{pb}^2$, $v_{teM} = v_{tb} = 0.01c$, and $A_e = A_b = 1$. Figure 3 shows real frequencies and growth rates for unstable modes in $\omega - k$ space. Four sets of upper and lower panels show the influence of varying the magnetic field, beam speed, beam density, and the temperature. The reference case is plotted by black lines in all the panels.

It is interesting to note that the instability property undergoes a gradual yet distinct change near the threshold corresponding to $\gamma_{\max} = \omega_{ce}$. That is, for $\gamma_{\max}$ higher than ω_{ce} in magnitude, it is seen that the growing modes turn into a continuous beam mode. As the maximum growth rate $\gamma_{\max}$ falls below ω_{ce}, however, the modes discretizes and take on the characteristics of Bernstein modes. Such a description is born out by all the cases considered in Figure 3 This behavior is not too difficult to understand, however, since the effects of the ambient magnetic field increasingly becomes important as the wave growth time scales exceed the inverse cyclotron period, ω_{ce}^{-1}.

Figure 3a shows the influence of varying ω_{ce}/ω_{pe} on the real frequency. It is seen that the unstable range monotonically decreases until it shrinks to a narrow range near F_{ce} Figure 3b shows that increasing ω_{ce}/ω_{pe} from the reference value of 0.1 leads to a reduction in the growth rate. As B field increases, the individual cyclotron harmonic structure associated with the growth rate becomes more distinct. In contrast, when ω_{ce}/ω_{pe} is reduced to 0.05, the growth rate envelop becomes a smooth curve, which resembles the unmagnetized beam-plasma instability growth rate.

Figure 3c shows that increasing beam speed steepens the beam mode curve in (ω, k) space, which is expected. Figure 3d, which plots the growth rate, indicates that decreasing/increasing the beam speed has a similar effect as increasing/decreasing B field intensity. That is, for higher beam speed the growth rate curve resembles the unmagnetized case in that individual harmonic peaks merge, while for lower beam speed, gyroharmonic peaks become more prominent.

Effects of varying beam density on the real frequency are generally quite small until the beam density is increase to $0.3N_0$, which is shown in Figure 3e. Figure 3f shows that decreasing beam density leads to the reduction in growth rate as well as more prominent harmonic structure. For beam density corresponding to $0.3N_0$, the growth rate increases significantly in magnitude, while the envelop becomes continuous. Note that the real frequency where the growth rate is maximum decreases to $\sim 0.6F_{pe}$ when the beam density is $0.3N_0$. Consequently, frequency ranges of growing modes can be an order of F_{ce} as in Event 2.

The effects of varying thermal speed are noteworthy. In general, the lower the thermal speed, the more continuous the growth rate curve becomes while increasing in magnitude. However, when thermal speed becomes very slow, $v_{tb} = v_{teM} = 0.005c$ and $0.004c$, separate branch(es) of unstable mode begin(s) to appear, as shown in the higher-k region of Figure 3g. This secondary (and tertiary) modes is (are) related to upper-hybrid waves from the core having slow thermal speeds. The envelop of growth rate curve in Figure 3h shows that the secondary unstable branch can be identified by small bumps at the high k domain. The tertiary branch, which is barely visible in the growth rate plot, can nonetheless be identified as well.
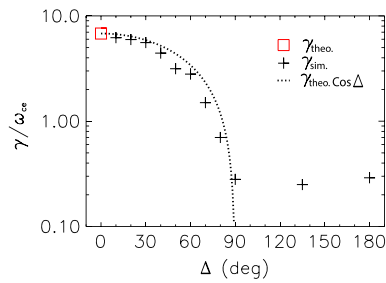
Figure 4. Dependence of the maximum growth rate on the broadening angle Δ. A Red square is the theoretical value of the reference (γ_{theo}), and black crosses come from PIC simulations using different values of Δ (γ_{sim}). The black dotted line is $\gamma_{theo} \times \cos \Delta$.

We further investigate the dependence of growth rates on the broadening angle (Δ) in the gyrophase space using 2-D PIC simulation, where Δ means that the crescent-shape electrons exist within the range of gyroangle from $-\Delta$ to $+\Delta$ forming a Maxwellian in the gyrospace centered at $\Delta = 0$. Therefore, the ring distribution corresponds to $\Delta = 180°$. Our theory assumes a delta function shape in the gyrophase space, and this assumption cannot be implemented by simulations. On the other hand, it is difficult to formulate and solve the theoretical dispersion relation with finite Δ distribution. Thus, theory and simulation are complementary. The particle loading and exchanging methods in Dokgo et al. (2019) are used to make crescent-shaped distributions.

We plot maximum growth rates derived from theory and simulation in Figure 4, where x axis represents the broadening angle Δ and y axis is the maximum growth rate γ/ω_{ce}. The red square denotes the theoretical maximum growth rate γ_{theo} of the reference case ($\Delta = 0$). Each black cross presents the maximum growth rate calculated from the slope of energy history of the E field in each simulation run using different Δ. The black dotted line is a multiplication of γ_{theo} and $\cos \Delta$. The growth rate from simulations converges to γ_{theo} as Δ approaches 0, which means that theory and simulation are in agreement. The maximum growth rate decreases as Δ increases. Their trend follows $\gamma_{theo} \times \cos \Delta$ (dotted line) when $\Delta < 90°$; however, it has a finite value when $\Delta = 90°$. In the range of $90° < \Delta \leq 180°$, the growth rate is not changed much.

The simulation results show that the effects of Δ on the growth rate, especially in the range of $60° < \Delta < 90°$, can be quite complex. In this range the simple formula $\theta_{theo} \times \cos \Delta$ predicts that the growth rate should rapidly decrease, as indicated by dotted curve. Instead, the growth rate deduced from simulations shows that the reduction in the growth is arrested and it gradually settles down to some finite level. We also found that gradual transition from the beam mode to Bernstein mode takes place as Δ increases, but we also found that the transition is rather smooth and not sudden (not shown). As can be seen from Figure 4, the growth rate crosses the threshold condition of $\gamma_{sim} = \omega_{ce} (= 0.1\omega_{pe})$ as Δ is varied such that our previously stated conclusion on the property of dispersion relations (see Figure 3) applies herewith. Recall that this threshold defines the transition from beam like to Bernstein mode.

4. Discussion and Conclusion

In this letter, we have investigated the detailed property associated with HFWs driven by agyrotropic electrons near the EDRs by employing MMS observations, kinetic theory, and PIC simulations. It was shown that these waves are basically discrete Bernstein modes when the effect of the ambient magnetic field is significant as in Event 2. As their growth rates increase depending on plasma parameters, each mode may overlap with adjacent modes. As a result, they may become a continuous beam mode as in Event 1.

We note that the types of reconnection, symmetric and asymmetric, are not the main reason for generations of different types of waves because upper-hybrid waves have been reported for both types of reconnection. However, different types of magnetic reconnection make different profiles of plasma parameters. Moreover, considering EDR environments, plasma parameters can vary depending on the locations of observations. Accordingly, various properties of HFWs could be detected near EDRs, such as broad frequency ranges from F_{ce} to F_{pe} and continuous or discrete structures, as shown above. Our theoretical approach thus shows that generations of those waves can be explained by a unified theory, and the underlying physics is the same. We have identified that the maximum growth rate $\gamma_{max} = \omega_{ce}$ could be a threshold condition that delineates one type of wave versus the other, namely, discrete versus continuous.

The amplitude of HFWs near EDRs can be extremely high, reaching up to 400 mV/m (Graham et al., 2017). Thus, HFWs can affect reconnection processes by energizing electrons effectively, which in turn may contribute to the origin of anomalous resistivity and viscosity. In addition, nonlinear processes of HFWs can generate electromagnetic radio emissions (Dokgo et al., 2019), which could, in principle, facilitate remote sensing of occurrences of magnetic reconnection. Consequently, investigating the properties of HFWs may be crucial for understanding the physics of EDRs and reconnection processes. Our study provides a more precise and unified treatment of HFWs driven by agyrotropic electrons near EDRs. With the help of quasi-linear

theory and kinetic simulation, future studies can quantitatively estimate anomalous resistivity and viscosity by HFWs in EDRs, which could eventually lead to the identification of energy conversion process in EDRs.

We have focused on electron phenomena near EDRs ignoring ions in this study, however, equation (1) is equally applicable for waves driven by agyrotropic ions. Since agyrotropic ions are ubiquitous in space, such as in ion diffusion regions of magnetic reconnection (Graham et al., 2017; Wang et al., 2016), the Earth's foreshock region (Eastman et al., 1981; Gosling et al., 1982), thin current sheets (Zhou et al., 2009), and near the space shuttle (Cairns, 1990), interactions between ion cores and agyrotropic ions are an important topic of fundamental plasma physics contributing energizations of both ions and electrons. Our work can provide detailed physics of generations of low-frequency waves, such as lower-hybrid waves or ion-acoustic waves, driven by gyrobunched ions.

References

Bessho, N., Chen, L. J., Shuster, J. R., & Wang, S. (2014). Electron distribution functions in the electron diffusion region of magnetic reconnection: Physics behind the fine structures. *Geophysical Research Letters*, *41*, 8688–8695. https://doi.org/10.1002/2014GL062034

Birn, J., Drake, J. F., Shay, M. A., Rogers, B. N., Denton, R. E., Hesse, M., et al. (2001). Geospace Environmental Modeling (GEM) magnetic reconnection challenge. *Journal of Geophysical Research*, *106*(A3), 3715–3719. http://doi.wiley.com/10.1029/1999JA900449

Burch, J. L., Dokgo, K., Hwang, K.-J., Torbert, R. B., Graham, D. B., Webster, J. M., et al. (2019). High frequency wave generation in magnetotail reconnection: Linear dispersion analysis. *Geophysical Research Letters*, *46*, 4089–4097. https://doi.org/10.1029/2019GL082471

Burch, J. L., Ergun, R. E., Cassak, P. A., Webster, J. M., Torbert, R. B., Giles, B. L., et al. (2018). Localized oscillatory energy conversion in magnetopause reconnection. *Geophysical Research Letters*, *45*, 1237–1245. https://doi.org/10.1002/2017GL076809

Burch, J. L., Moore, T. E., Torbert, R. B., & Giles, B. L. (2016). Magnetospheric Multiscale overview and science objectives. *Space Science Reviews*, *199*(1-4), 5–21. https://doi.org/10.1007/s11214-015-0164-9

Burch, J. L., Torbert, R. B., Phan, T. D., Chen, L. J., Moore, T. E., Ergun, R. E., et al. (2016). Electron-scale measurements of magnetic reconnection in space. *Science*, *352*(6290), aaf2939. http://www.sciencemag.org/lookup/doi/10.1126/science.aaf2939

Cairns, I. H. (1989). Electrostatic wave generation above and below the plasma frequency by electron beams. *Physics of Fluids B*, *1*(1), 204–213.

Cairns, I. H. (1990). Transition from ring to beam arc distributions of water ions near the Space Shuttle Orbiter. *Journal of Geophysical Research*, *95*(A9), 15167. https://doi.org/10.1029/JA095iA09p15167

Dokgo, K., Hwang, K.-J., Burch, J. L., Choi, E., Yoon, P. H., Sibeck, D. G., & Graham, D. B. (2019). High-frequency wave generation in magnetotail reconnection: Nonlinear harmonics of upper hybrid waves. *Geophysical Research Letters*, *46*, 7873–7882. https://doi.org/10.1029/2019GL083361

Eastman, T. E., Anderson, R. R., Frank, L. A., & Parks, G. K. (1981). Upstream particles observed in the Earth's foreshock region. *Journal of Geophysical Research*, *86*(A6), 4379–4395. https://doi.org/10.1029/JA086iA06p04379

Egedal, J., Wetherton, B., Daughton, W., & Le, A. (2016). Processes setting the structure of the electron distribution function within the exhausts of anti-parallel reconnection. *Physics of Plasmas*, *23*(12).

Ergun, R. E., Tucker, S., Westfall, J., Goodrich, K. A., Malaspina, D. M., Summers, D., et al. (2016). The axial double probe and fields signal processing for the MMS mission. *Space Science Reviews*, *199*(1-4), 167–188. https://doi.org/10.1007/s11214-014-0115-x

Gosling, J. T., Thomsen, M. F., Bame, S. J., Feldman, W. C., Paschmann, G., & Sckopke, N. (1982). Evidence for specularly reflected ions upstream from the quasi-parallel bow shock. *Geophysical Research Letters*, *9*(12), 1333–1336. https://doi.org/10.1029/GL009i012p01333

Graham, D. B., Khotyaintsev, Y. V., Norgren, C., Vaivads, A., André, M., Toledo-Redondo, S., et al. (2017). Lower hybrid waves in the ion diffusion and magnetospheric inflow regions. *Journal of Geophysical Research: Space Physics*, *122*, 517–533. https://doi.org/10.1002/2016JA023572

Graham, D. B., Khotyaintsev, Yu. V., Vaivads, A., Norgren, C., André, M., Webster, J. M., et al. (2017). Instability of agyrotropic electron beams near the electron diffusion region. *Physical Review Letters*, *119*(2), 025101. https://doi.org/10.1103/PhysRevLett.119.025101

Graham, D. B., Vaivads, A., Khotyaintsev, Yu. V., André, M., Le Contel, O., Malaspina, D. M., et al. (2018). Large-amplitude high-frequency waves at Earth's magnetopause. *Journal of Geophysical Research*, *123*, 2630–2657. https://doi.org/10.1002/2017JA025034

Hesse, M., Aunai, N., Sibeck, D., & Birn, J. (2014). On the electron diffusion region in planar, asymmetric, systems. *Geophysical Research Letters*, *41*, 8673–8680. https://doi.org/10.1002/2014GL061586

Hesse, M., & Winske, D. (1994). Hybrid simulations of collisionless reconnection in current sheets. *Journal of Geophysical Research*, *99*(A6), 11,177–11,192. https://doi.org/10.1029/94JA00676

Li, W. Y., Graham, D. B., Khotyaintsev, Y. V., Vaivads, A., André, M., Min, K., et al. (2020). Electron Bernstein waves driven by electron crescents near the electron diffusion region. *Nature Communications*, *11*(1), 141.

Lindqvist, P. A., Olsson, G., Torbert, R. B., King, B., Granoff, M., Rau, D., et al. (2016). The spin-plane double probe electric field instrument for MMS. *Space Science Reviews*, *199*(1-4), 137–165. https://doi.org/10.1007/s11214-014-0116-9

Lyons, L. R., & Pridmore-Brown, D. C. (1990). Force balance near an X line in a collisionless plasma. *Journal of Geophysical Research*, *95*(A12), 20,903–20,909. https://doi.org/10.1029/JA095iA12p20903

Paschmann, G., Daly, P. W., Sonnerup, B. U. Ö., Scheible, M., & Khrabrov, A. V. (1998). *Analysis methods for multi-spacecraft data Edited by* Paschmann, G., & Daly, P. W. Bern, Switzerland: International Space Science Institute. SR-001.

Pollock, C., Moore, T., Jacques, A., Burch, J., Gliese, U., Saito, Y., et al. (2016). Fast Plasma Investigation for Magnetospheric Multiscale. *Space Science Reviews*, *199*(1-4), 331–406. https://doi.org/10.1007/s11214-016-0245-4

Romeiras, F. J., & Brinca, A. L. (1999). On the stability of perpendicular electrostatic modes in stationary nongyrotropic plasmas. *Journal of Geophysical Research*, *104*(A6), 12,407–12,413. http://doi.wiley.com/10.1029/1999JA900101

Russell, C. T., Anderson, B. J., Baumjohann, W., Bromund, K. R., Dearborn, D., Fischer, D., et al. (2016). The Magnetospheric Multiscale Magnetometers. *Space Science Reviews*, *199*(1-4), 189–256. https://doi.org/10.1007/s11214-014-0057-3

Scudder, J., & Daughton, W. (2008). Illuminating electron diffusion regions of collisionless magnetic reconnection using electron agyrotropy. *Journal of Geophysical Research*, *113*, A06222. https://doi.org/10.1029/2008JA013035

Shuster, J. R., Shuster, J. R., Chen, L. J., Hesse, M., Argall, M. R., Argall, M. R., et al. (2015). Spatiotemporal evolution of electron characteristics in the electron diffusion region of magnetic reconnection: Implications for acceleration and heating. *Geophysical Research Letters*, *42*, 2586–2593. https://doi.org/10.1002/2015GL063601

Tang, B. B., Li, W. Y., Graham, D. B., Rager, A. C., Wang, C., Khotyaintsev, Y. V., et al. (2019). Crescent-shaped electron distributions at the nonreconnecting magnetopause: Magnetospheric Multiscale observations. *Geophysical Research Letters*, *46*, 3024–3032. https://doi.org/10.1029/2019GL082231

Vasyliunas, V. M. (1975). Theoretical models of magnetic field line merging. *Reviews of Geophysics*, *13*(1), 303–336.

Wang, S., Chen, L.-J., Hesse, M., Bessho, N., Gershman, D. J., Dorelli, J., et al. (2016). Two-scale ion meandering caused by the polarization electric field during asymmetric reconnection. *Geophysical Research Letters*, *43*, 7831–7839. https://doi.org/10.1002/2016GL069842

Zhou, X.-Z., Angelopoulos, V., Runov, A., Sitnov, M. I., Coroniti, F., Pritchett, P., et al. (2009). Thin current sheet in the substorm late growth phase: Modeling of THEMIS observations. *Journal of Geophysical Research*, *114*, A03223. https://doi.org/10.1029/2008JA013777